On the Creation, Depletion, and End of Life of Polar Cap Patches

Nina Kristine Eriksen[1,2], Dag Lorentzen [1,2], Kjellmar Oksavik [1,2], Lisa Baddeley [1,2], Keisuke Hosokawa [3], Kazuo Shiokawa [4], Emma Bland [1], Larry Paxton [5], Yongliang Zhang [5], Kathryn McWilliams [6], and Tim Yeoman [7]

[1]Department of Arctic Geophysics, The University Centre in Svalbard, Longyearbyen, Norway
[2]Birkeland Centre for Space Science, Department of Physics and Technology, University of Bergen, Bergen, Norway
[3]Department of Communication Engineering and Informatics, University of Electro-Communications, Tokyo, Japan
[4]Institute for Space-Earth Environmental Research, Nagoya University Furo-cho, Nagoya, Japan
[5]The Johns Hopkins University Applied Physics Laboratory, Laurel, USA
[6]Department of Physics and Engineering Physics, University of Saskatchewan, Saskatoon, Canada
[7]University of Leicester, School of Physics and Astronomy, Leicester, UK.

Key Points:

- Tracking of high-density plasma volumes in the ionosphere is a viable tool for uniting spatially distant observations
- A drifting polar cap patch has variable plasma decay rate at different stages of its lifetime
- Stagnation of a polar cap patch is considered a major determinant for a complete decay

Corresponding author: Nina Kristine Eriksen, ninae@unis.no

Abstract

Ionospheric convection patterns from the Super Dual Auroral Radar Network are used to determine the trajectories, transit times and decay rates of three polar cap patches from their creation in the dayside polar cap ionosphere to their end of life on the nightside. The first two polar cap patches were created within 12 minutes of each other and travelled through the dayside convection throat, before entering the nightside auroral oval after 104 and 92 minutes, respectively. When the patches approached the nightside auroral oval, an intensification in the poleward auroral boundary occurred close to their exit point, followed by a decrease in the transit velocity. The airglow decay rates of patches 1 and 2 were found to be ≈0.6% and ≈0.9% per minute, respectively. The third patch decayed completely within the polar cap and had a lifetime of only 78 minutes. After a change in drift direction, patch 3 had a radar backscatter power half-life of 4.23 minutes, which reduced to 1.80 minutes after a stagnation, indicating a variable decay rate. 28 minutes after the change in direction, and 16 minutes after stagnation, patch 3 completely disintegrated. We relate this rapid decay to increased frictional heating, which speeds up the recombination rate. Therefore, we suggest that the stagnation of a polar cap patch is a main determinant to whether or not a polar cap patch can exit through the nightside auroral oval.

1 Introduction

Polar cap patches (PCPs) are isolated, dense segments in the F-region of the ionosphere with enhanced plasma densities at least twice that of the ambient plasma (Weber et al., 1984; Crowley, 1996; Carlson, 2012). The plasma source of the PCPs often comes from dayside subauroral latitudes where a reservoir of enhanced plasma is produced by photoionization from solar EUV radiation. However, particle precipitation in the cusp and polar cap can also contribute to patch formation (Rodger et al., 1994; Walker et al., 1999; Lockwood et al., 2005; Oksavik et al., 2006; Goodwin et al., 2015). The study of the complete transit of PCPs from their creation to their end of life is often a complicated process due to scarce data coverage. PCPs travel with the convection velocity, however this flow is often turbulent at the meso-scale level and the influence on the PCP structure and transit path across the polar cap is still under discussion. The optical signature of PCPs is known as airglow patches, which often occur after the optical signature of pulsed reconnection, namely poleward moving auroral forms (PMAFs) (Sandholt et

al., 1986; Southwood, 1987; Sandholt et al., 1998, 2004). Airglow patches are mainly seen as 630.0 nm airglow emissions (as opposed to 630.0 nm auroral emissions) since the light stems from de-excitation of atomic oxygen around 250 km altitude (Hays et al., 1978):

$$O^*(^1D) \rightarrow O(^3P) + hv_{630.0nm} \tag{1}$$

There are several case studies of airglow patches (Weber et al., 1984; Hosokawa et al., 2009; Perry et al., 2013; Zou et al., 2015; Hosokawa et al., 2016), but only a few reports have corresponding electron density measurements (cf. Lorentzen et al., 2010). Recent studies that have successfully followed patches for most of their lifetime across the polar cap are Oksavik et al. (2010), Q. H. Zhang et al. (2013), Nishimura et al. (2014), Spicher et al. (2015), Thomas et al. (2015), and Hwang et al. (2020).

Oksavik et al. (2010) used the EISCAT Svalbard Radar (ESR) (Wannberg et al., 1997) and the Super Dual Auroral Network (SuperDARN) (Greenwald et al., 1995; Chisham et al., 2007; Nishitani et al., 2019) to study the transit of two extreme electron density events ($n_e > 10^{12}\mathrm{m}^{-3}$). They found that the two events underwent a substantial rotation as they crossed the polar cap and were observed to have pulsed flow speeds. Nishimura et al. (2014) conducted a study of patch propagation across the polar cap using SuperDARN and all-sky camera measurements and reported a PMAF which evolved into a polar cap airglow patch on the dayside. They followed the airglow patch through optical measurements and observed a fast flow channel coincident with the airglow patch through polar boundary intensification and localized reconnection on the nightside.

Although SuperDARN measurements and other instruments have previously been able to track PCPs for their entire lifetime, there is still a need for a more generalized tracking method that is not solely dependent on extreme events or optimal observation alignment. PCPs are considered a space weather challenge (Moen et al., 2013; Van Der Meeren et al., 2014; Jin et al., 2014; Oksavik et al., 2015), due to their ability to disrupt signals from global navigation satellite systems, which can be detrimental at polar latitude. Therefore, a robust tracking method would be an important application for forecasting PCP trajectories. In addition, successful tracking of PCPs allows us to study changes to their morphology by uniting observations at various stages of their lifetime. The electron density decay rate throughout a patch's lifetime is still up for debate. Only a few studies have addressed the electron density decay rate of PCPs or small-scale plasma structures ($\sim$1km) in the F-region (Hosokawa et al., 2011; Ivarsen et al., 2021).

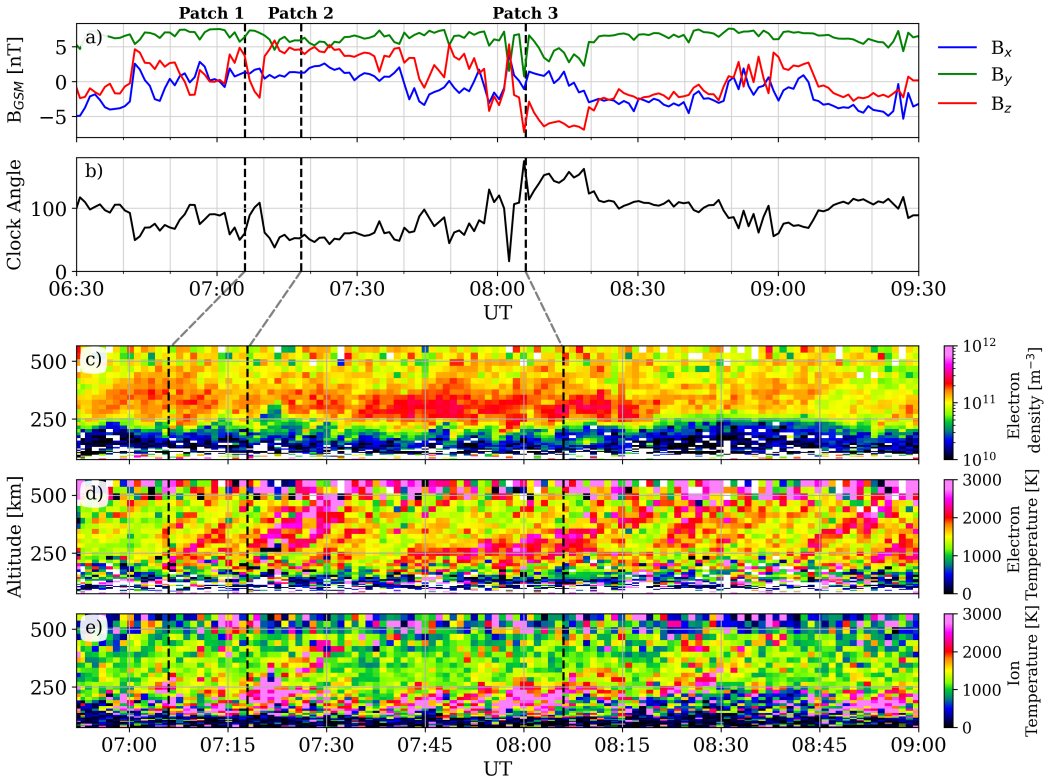

Figure 1. a) Interplanetary magnetic field measurements from ACE and b) shows corresponding clock angles on 19 December 2014. c) shows ESR 32m electron number density, and d) and e) show ESR 32m electron and ion temperatures, respectively. Release times for patches 1, 2, and 3 are seen as vertical, dashed lines.

This paper presents several PCPs detected by the ESR (78.15^{o}N, 16.1^{o}E) on 19 December 2014. We follow three patches across the polar cap. Their trajectories are determined from SuperDARN convection maps and confirmed optically by measurements of airglow patches seen over Ny Ålesund (78.92^{o}N, 11.93^{0}E) and Resolute Bay (74.73 ^{o}N, 265.07^{o}E), as well as backscatter echos from individual SuperDARN radars from Hankasalmi, Clyde River, Rankin Inlet, and Inuvik. Two of the patches transited the entire polar cap and entered the auroral oval near magnetic midnight. The third patch rotated after passing the magnetic pole and did not exit the polar cap before it dissipated in the nightside dawn convection cell.

2 Instrumentation and Data Presentation

2.1 Solar Wind and Magnetic Data

The NASA Advanced Composition Explorer satellite (ACE) was located at the L1 Lagrangian point and provides data for the solar wind and interplanetary magnetic field (IMF) conditions. In Figure 1 a) and b) the IMF components and the clock angle measurements are given for the period 06:30 to 09:30 UT, respectively. On 19 December 2014 we observe a generally steady and strong positive IMF By, together with a positive clock angle around 100^o, as well as some changes in the north-south IMF direction. The solar wind velocity was steady around 350-400 km/s, and the proton density was, for the most part, around 3.6 cm^{-3}, with a single spike above 8 cm^{-3} at 08:10 UT (data not shown). The solar wind data are presented in Figure 1 a) and b), with a 70-minute time shift from L1 to the dayside ionosphere, which was found using mean solar wind velocity and dayside aurora activity. The relevant time period on 19 December 2014 had no geomagnetic storm activity with SYM-H > -25nT and a Kp-index between 1 and 2.

The Defense Meteorological Satellite Program (DMSP) SSUSI LHBS auroral image (Paxton & Meng, 1999; Paxton et al., 2002; Paxton & Zhang, 2016) and SSIES Horizontal ion velocity is presented in Figure 2 a). The data is from the F16 pass as the satellite was crossing the polar cap. It passed over Svalbard between 06:52 and 06:54 UT. The data provides a large-scale context of the auroral oval and the ionospheric flow immediately prior to the time of interest in this paper. The figure shows that Svalbard (78^oN, 16^oE geographic) is located within the polar cap due to the expanded oval, with an antisunward flow direction in the pre-noon polar cap, which is consistent with positive IMF By.

2.2 European Incoherent Scatter Svalbard Radar

The ESR steerable 32m dish was measuring at a low elevation of 30^o and an azimuth direction of 331^o (where 0^o is at geographic north) on 19 December 2014. The radar provided measurements of the ionospheric parameters; electron density, electron temperature and ion temperature, presented in Figure 1 c)-e), respectively. The field-of-view (FOV) of the radar is presented as a solid black line in Figure 2 b).

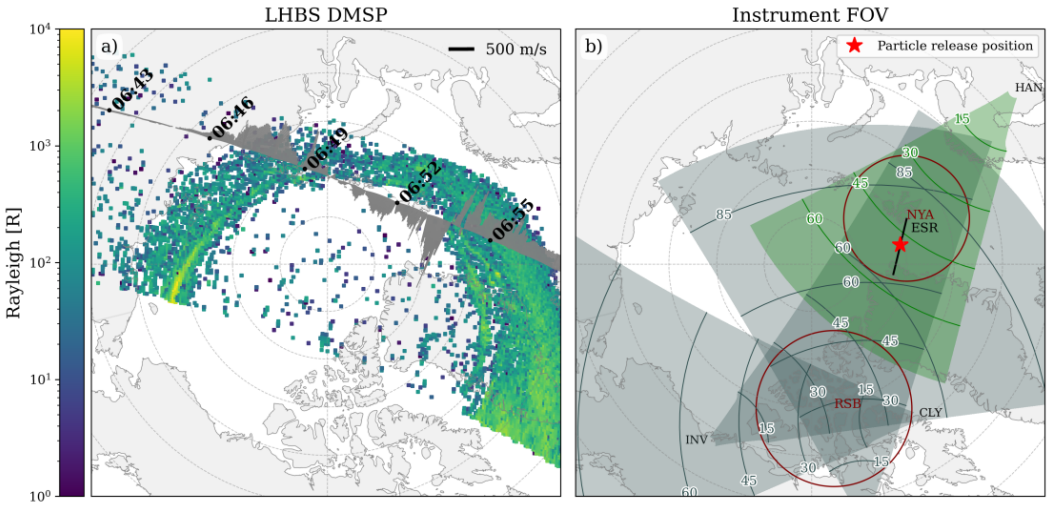

Figure 2. a) Measurements of the auroral oval from DMSP SSUSI auroral data (LHBS) and SSIES horizontal ion velocity at 06:43-06:59 UT in geographical coordinates. b) Field-of-view of the individual SuperDARN radars: Hankasalmi (HAN) is shown in green, and Inuvik (INV), Rankin Inlet (RKN) and Clyde River (CLY) are shown in gray. The field-of-view of the two all-sky imagers located at Ny Ålesund (NYA) and Resolute Bay (RSB) are seen as maroon circles. The location of the 32m EISCAT Svalbard Radar beam is shown as a black line. The location where the particles were released for tracking across the polar cap is marked with a red star. The locations are all given in geographical coordinates.

2.3 All-sky Imagers: 630.0 nm Emission

The optical measurements presented in this study are provided from two all-sky imagers (ASIs) equipped with 630.0 nm narrow bandpass interference filters. The ASI located in Ny Ålesund (NYA) is owned by the University of Oslo (UiO) and provides images mapped to 250 km altitude for elevation angles above 19^o. Images from the Resolute Bay Optical Mesosphere Thermosphere Imagers ASI (RSB) are mapped to 230 km altitude with measurements above 20^o elevation angles (Shiokawa et al., 1999, 2009). The mapping altitudes correspond to the expected altitudes for de-excitation of atomic oxygen, and thus airglow emissions. Both camera FOVs are presented in Figure 2 b) as maroon circles.

For all ASI images, the background is removed using a one-hour running average in order to focus on weaker perturbations in the airglow intensity. The images are subsequently converted to relative intensity using the same one-hour running average. Finally, they are presented as a percentage relative to a background intensity:

$$100 \cdot (I_{measured} - I_{backgr})/I_{backgr} \tag{2}$$

where I_{backgr} is the one-hour running average representing the background intensity.

2.4 Super Dual Auroral Radar Network

Ionospheric convection patterns determined from the SuperDARN radars were used to estimate the trajectories of the three patches over the polar cap. The convection patterns were determined using the SuperDARN Radar Software Toolkit (RST)(SuperDARN Data Analysis Working Group. et al., 2021). The data had been processed from the raw radar data using the standard SuperDARN fitting algorithm called FitACF3.0 to estimate the line-of-sight (LOS) velocity parameter. Additional tools in the RST were then used to combine the IMF data provided in section 2.1 and data from all northern hemisphere radars onto a grid of equal-area cells spanning 1^o of magnetic latitude, and then determine the convection pattern using the standard SuperDARN "Map Potential" algorithm (Ruohoniemi & Baker, 1998).

In addition to the northern hemisphere convection patterns, backscatter power and LOS velocity measurements from the SuperDARN radars at Hankasalmi, Inuvik, Rankin Inlet and Clyde River were used to identify and track the PCPs at various locations in

the polar cap. The FOV of these radars are shown in Figure 2 b). These data were also processed using the FitACF3.0 fitting algorithm in the RST.

3 PCP Tracking Method

3.1 Virtual Particle Tracking with SuperDARN Data

A simple particle tracking method was developed using a geomagnetic (MLAT, MLON) reference system. Given the initial release coordinates, the SuperDARN convection maps were used to calculate the subsequent particle location using the velocity vectors. A particle at position a with speed v_a and azimuth angle k_a was used to give the next latitude and longitude coordinates at position b through the Haversine formula for great-circle distance. The process was repeated for 4 hours with a time cadence of 2 minutes. Repeatedly releasing particles between 06:50 and 08:30 UT, which correspond to the period of higher density seen in Figure 1 c), allowed us to determine release times for the three PCP events.

The initial release location in geographical coordinates was 80.42^{o}N and -1.64^{o}E, corresponding to the ESR beam at 281km altitude. The release altitude was chosen close to the median altitude for the electron density peak in the F-region between 06:00-12:00 UT and based on the best fit between the virtual particle trajectories and the observed airglow patches. Choosing a different initial release location could lead to a clear difference in the resulting trajectories as flow shears could send the particles into different directions.

3.2 Event Selection

The three PCP events were selected based on: 1) ESR measurement of high density in F-region and no significant temperature enhancements i.e., temperature enhancement not related to the PMAF, 2) patch production/source features in the vicinity on the dayside, i.e. PMAFs or tongue of ionization (TOI) (cf. Foster et al., 2005) as observed by the UiO ASI and TEC measurements from satellites (not shown), 3) simultaneous observations of airglow patch movement, and 4) simultaneous observations of strong backscatter power in the individual SuperDARN radars, preferable Clyde River and Inuvik due to their favorable FOV orientation.

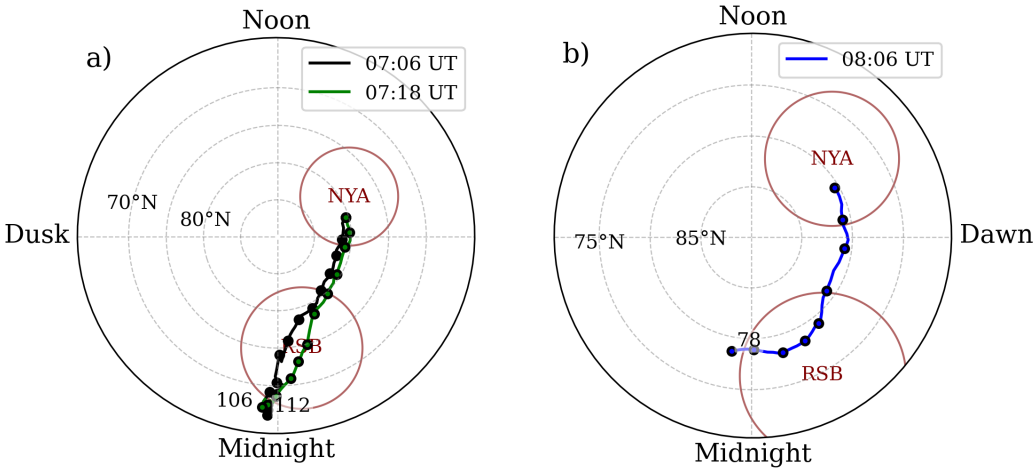

Figure 3. a) and b) show the trajectories of the virtual particles released at 07:06 and 07:28 UT, and 08:06 UT respectively. Each 10^{th} minute of the trajectories, in addition to the first and final minutes, are marked as black rings. The Ny Ålesund (NYA) and Resolute Bay (RSB) camera FOVs are shown in maroon.

4 Results

Using the selection criteria outlined in the above section, three trajectories were chosen, patch 1 (P1), patch 2 (P1), and patch 3 (P3). From Figure 1 c) P1 and P2 have lower electron densities than P3 and appear more isolated. The low elevation angle of the ESR means that a poleward motion of the patches (along the look direction of the radar beam) manifests itself as an apparent altitude increase as a function of time, resulting in the "slanted" shape of the structures. P3 has a higher electron density and stems from a time with more continuous, high-density plasma passing over the ESR. The measurements indicate that the patches originate from the TOI; denser Solar-EUV ionospheric plasma transported from lower latitudes into the polar cap. There are no significant temperature increases seen in the ESR for the three patches, suggesting high density isolated volumes that migrate into the polar cap. TEC maps show high density and high phase scintillation, indicating dense, structured plasma in the F-region (not shown).

4.1 Multimedia Material

This paper is accompanied by two videos, one embedded and supplementary. It is strongly encouraged to watch Video 1 before reading the rest of the paper, as this video

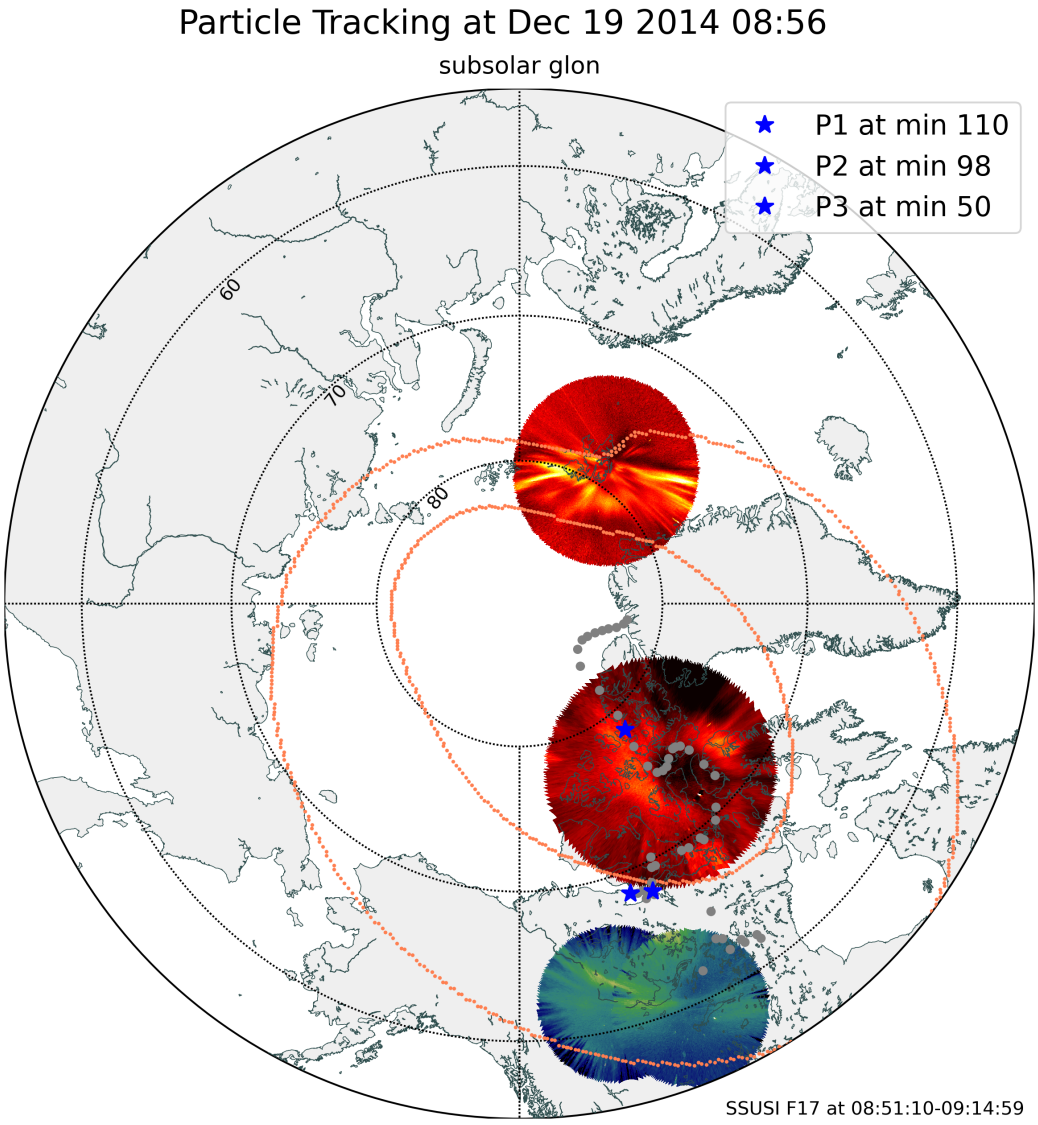

Video 1. Shows the tracking of the virtual particles released between 06:50 and 08:30 UT in geographical coordinates. The selected events are shown as blue stars and the remaining as gray dots. The DMSP SSUSI auroral boundaries are shown in coral. All-sky images (630.0 nm filtered) from Ny Ålesund and Resolute Bay, as well as images from Fort Smith and Fort Simpson (557.7 nm filtered) are also included. The placeholder image is from 31 seconds into the video.

provides a dynamical presentation of the airglow patches, the auroral oval and the motion of the selected events. Video 1 presents virtual particles released every second minute between 06:50 and 08:30 UT and their geographic locations in the polar cap. The selected events are presented as blue stars, the remaining virtual particles as gray dots. Corresponding ASI 630.0 nm images from NYA and RSB are included. In addition, ASI images from Fort Smith and Fort Simpson, which are both equipped with 557.7 nm narrow bandpass interference filters, from the history of events and macroscale interactions during substorms (THEMIS) network were included in Video 1 to investigate potential auroral interactions in the nightside auroral boundary as the PCPs traversed the nightside polar cap. Also included, when available, are the DMSP SSUSI modeled poleward and equatorward auroral boundaries, shown in coral, to provide a proxy for the auroral oval (Y. Zhang & Paxton, 2008). The satellite number and swath time is presented at the bottom of each frame.

The airglow patches were identified using Video 1 and raw ASI images from NYA and RSB (not shown). In Video 1, week airglow patches corresponding to P1 and P2 can be seen at the north-western edge of the NYA FOV after the corresponding PMAF has retreated. Next, the airglow patches enter the north-eastern RSB FOV. As the airglow patches move towards the FOV center high-intensity, small-scale arc-like structures can be seen embedded within the patches. P3's airglow patch also exits the north-western edge of the NYA FOV, before it appears in the north-eastern RSB FOV.

Supplementary Video 1 (Video S1) presents the location of P1, P2, and P3 (red stars) as they transit the polar cap in the geomagnetic reference frame. The convection velocity maps, seen as the underlaying color-map, from SuperDARN RST processing are included to provide information on the ionospheric convection. The video does not include the LOS velocities for the northern hemisphere, but instead includes the fitted vector velocities, seen as dots with respective vector lines. Also seen, in coral, are the DMSP SSUSI auroral boundaries. Going forth, data from convection velocity maps are referred to as convection model velocity, model velocity or Px velocity.

4.2 Patch 1 & 2: Release Times at 07:06 & 07:18 UT

Because P1 and P2 show many similarities they will be presented together. In Video 1 an intensification in the aurora on the dayside can be seen at 06:58 UT, followed by

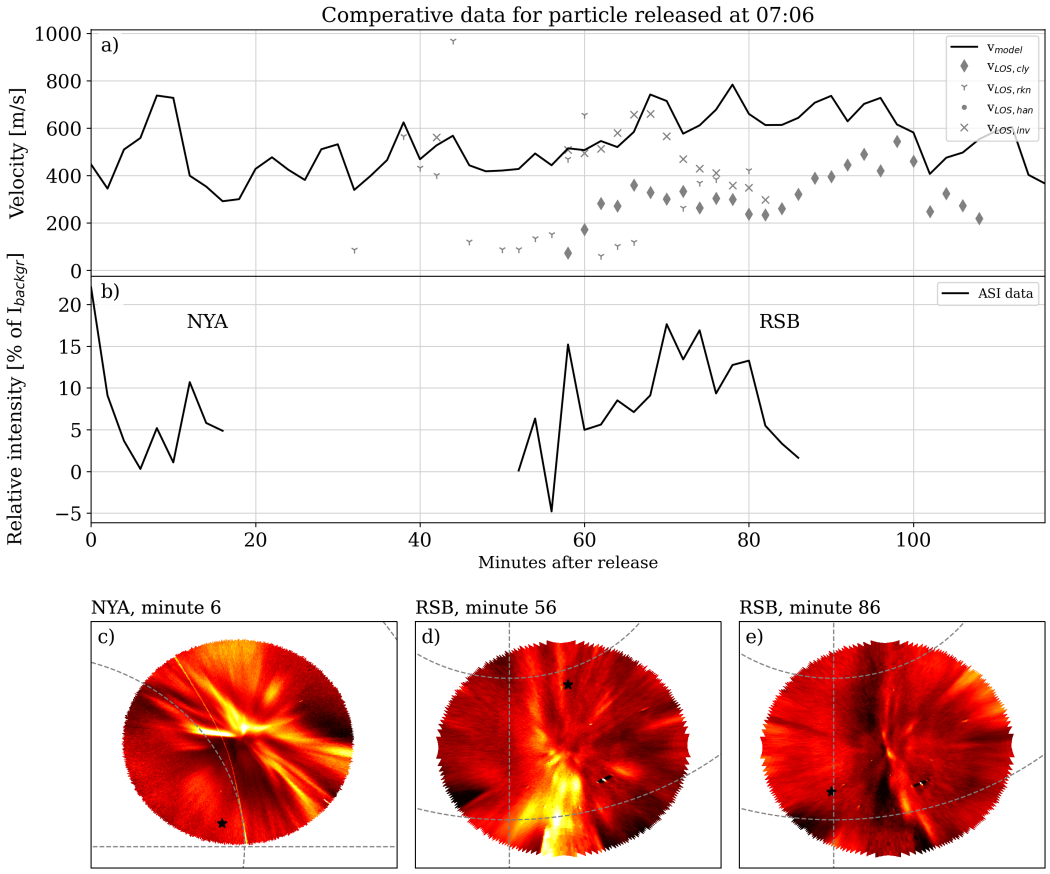

Figure 4. Results for patch 1, released at 07:06 UT, during its trajectory across the polar cap. Panel a) shows the convection velocity at each step in the transit and the individual radar LOS velocities that were within 100 km of the virtual particle position. Panel b) shows the relative emission intensity at the particle's position, where available, compared to a one-hour running mean of the background intensity. c) Shows a Ny Ålesund ASI image at minute 6 of the trajectory, and d)-e) show Resolute Bay ASI images at minutes 56 and 86, respectively. The star represents the tracking location at the time. The orientation of the cameras is shown in Figure 3 a)

a PMAF that disappears at 07:16 UT. At 07:06 UT the virtual particle was released representing P1. P2 was released during a PMAF, which started with an intensification at 07:12 UT and moved poleward until 07:36 UT. Figure 1 c) shows an elevated electron density during both release times.

Both P1 and P2 move across the polar cap within the convection throat (See Video S1), and their trajectories are presented in Figure 3 a). DMSP SSUSI auroral boundaries, auroral oval activity seen in 557.7 nm filtered ASI images from Fort Smith and Fort Simpson indicate that P1 and P2 have already entered the nightside auroral oval at minute 104 and 92 (08:50 UT), respectively. From minute 94 and 82 (08:40 UT) for P1 and P2, respectively, intensifications in the nightside auroral can be seen in Video 1. The intensifications occur several times until the end of both patches' lifetime.

In Figure 4 a) we present the P1 velocity determined from the convection pattern as it transits the polar cap, seen as a line. The markers show the LOS velocity measurements of individual radars within 100 km of P1. Panel b) presents the relative intensity with respect to a one-hour running mean background intensity of the NYA and RSB cameras. The intensity was collected at the position of P1, given that the measurements elevation angle was larger than 20^o. Figures 4 c) - e) show ASI images from NYA and RSB for different minutes in the P1 trajectory. Figure 4 c) shows the location of P1 at minute 6 in the newly created airglow patch after the PMAF has disappeared. Figures 4 d) and e) show the airglow patch recently entering and close to leaving the RSB FOV at minute 56 and 86, respectively.

Figures 4 a) and b) show no clear correlation between the velocity of P1 and the relative intensity. In the first 20 minutes panel a) shows variable velocity ranging from below 300 m/s to almost 750 m/s, however the next 40 minutes shows a fairly steady velocity around 500 m/s as P1 moves across the polar cap. The velocity increases steadily after minute 60, before it starts decreasing at minute 96. The decrease in velocity coincides with the intensifications seen in the nightside auroral oval.

In panel b) an increase in the intensity can be seen as P1 moves into the RSB FOV. The intensity increases until minute 70, before it starts decreasing again as P1 moves towards the southern FOV boundary. There is a total decrease of $\approx 16\%$ but limiting the lowest elevation angle to 30^o (minute 78) to account for unfavorable measuring geometry, the total decrease in relative intensity is $\approx 5\%$ or 0.625% per minute. In Video 1

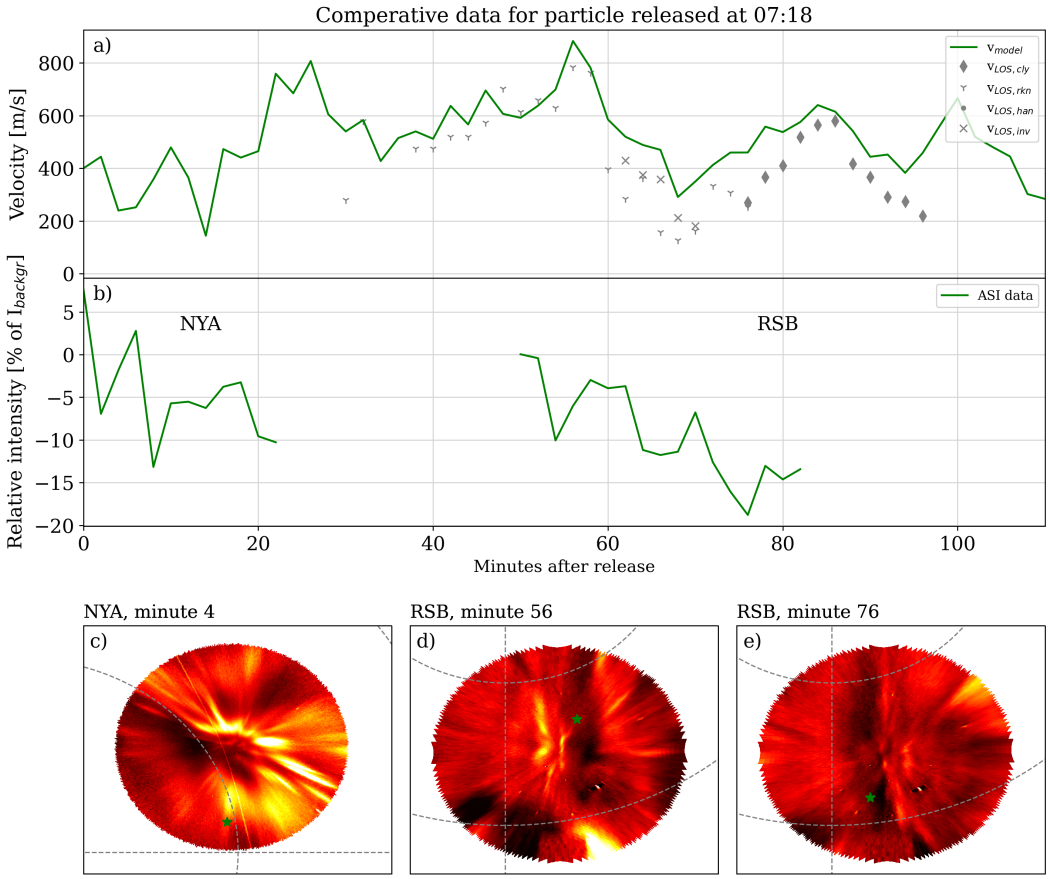

Figure 5. Same format as figure 4, but for patch 2 released at 07:18 UT.

small, arc-like structures, can be seen between minute 32 and 88 (07:38 and 08:34 UT) in the RSB FOV. These structures are also presented in Figures 4 d) and e). Since the ASI measures both aurora and airglow, the airglow decay rate of P1 could include a contribution from aurora e.g., from small-scale auroral-arcs.

P2 shows a more variable and pulsed velocity compared to P1, varying from around 144 m/s to around 880 m/s during the transit, see Figure 5 a). In the second half of the transit a maximum velocity of 880 m/s can be seen at minute 56, before it decreases to 286 m/s at minute 68. During this period there is a decrease in relative intensity (panel b), but the velocity increases to 638 m/s at minute 84, whereas the intensity continues to decrease. Thus, there is no clear correlation between the P2 velocity and the relative intensity. Like P1, the decrease in velocity seen at minute 84 coincides with the intensities seen in the nightside auroral oval.

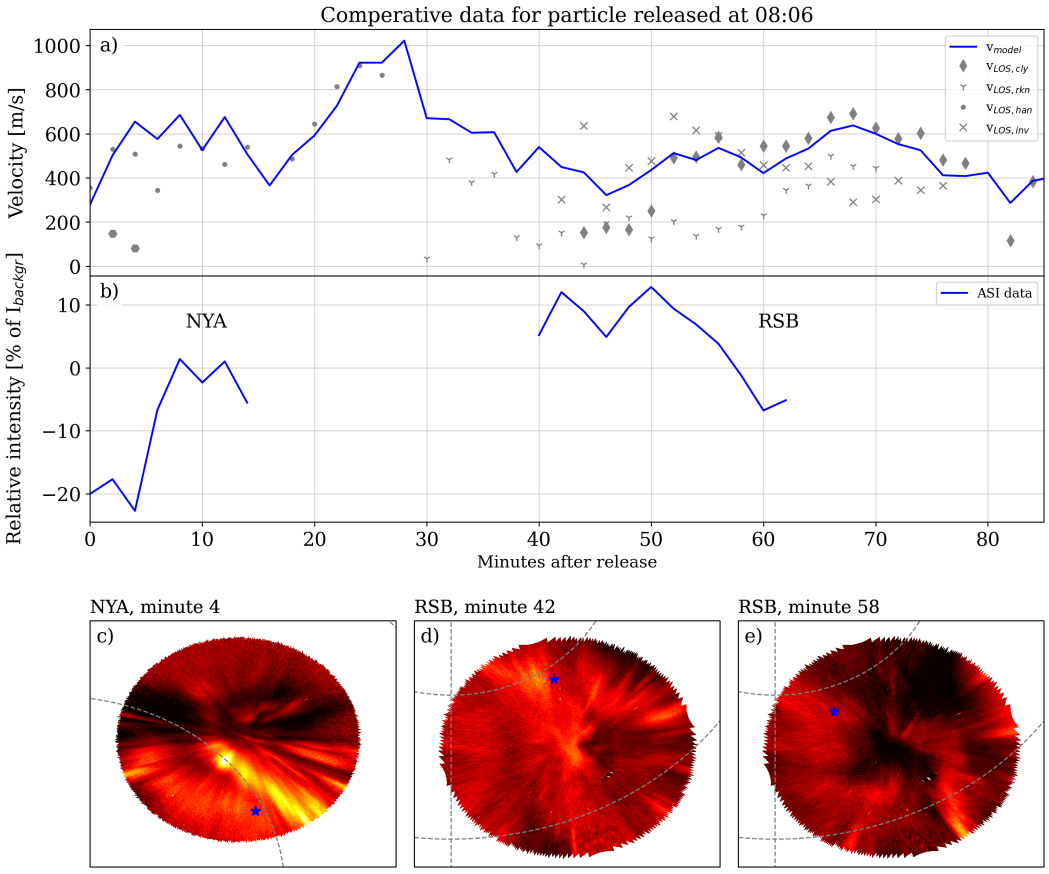

Figure 6. Same format as figure 4, but for patch 3 released at 08:06 UT. The orientation of the cameras is as seen in 3 b).

As seen in Figure 5 b), there is a decrease in relative intensity after 50 minutes. The total decrease from the highest relative intensity at minute 58 to the lowest at minute 76 is $\approx 16\%$ or 0.89% per minute. In Figure 5 c)-e) we present ASI images from NYA and RSB during minute 4, 56, and 76, respectively. In panel c) P2 is still within the PMAF it was released into, and in panel d) and e) we can see the small-scale aurora arc-like structures embedded within the airglow patch.

4.3 Patch 3: Release Time at 08:06 UT

Video 1 shows high activity, and a brightening of the dayside auroral oval at 07:50 UT, followed by a PMAF observed until 08:12 UT. However, the PMAF seems to be more intense with a brightening moving westward in the camera FOV, instead of a typical initial brightening at the equatorward boundary as seen for P1 and P2. Figure 3 b) shows

that there is a change in the direction of motion of P3. Initially, P3 moves within the convection throat, before a rotation occurs around minute 50. Afterwards, P3 drifts towards dusk and does not appear to leave the polar cap.

In Figure 6 a) the P3 velocity increases till it reaches a maximum of over 1000 m/s at minute 28, before it hits a minimum of 321 m/s at minute 46. The next 22 minutes the velocity increases again before another decrease occurs. Between minute 52 and 78, the LOS velocities measured by Clyde River radar are very close to the model velocities. This suggests that P3 was moving parallel to the radar beam during this time. Figure 6 b) shows a decrease in emission intensity from minute 50 to 60, after a period of high intensity, which appears to correspond to the second velocity increase seen in panel a). In Video 1 there is no indication of auroras as the airglow patch corresponding to P3 moves within the RSB FOV. This can be seen in Figures 6 d) and e), which shows the airglow patch at the intensity maximum at minute 42 and a dimmer airglow patch at minute 58.

Figures 7 a) and b) show the radar backscatter power and LOS velocity, respectively, as P3 travels along Clyde River beam 14 as it nears its end of life. Figures 7 c)-k) show the movement of P3 (outlined in green, which was determined by eye). It first enters the Clyde River radar FOV at minute 40 (08:46 UT) from the north-east, and at minute 50 (08:56 UT) it moves westward along beam 14, before a stagnation occurs at minute 62 (09:08 UT). At around minute 70 (09:16 UT) the patch appears to start breaking up, which corresponds to a rapid decrease of backscatter power in Figure 7 a), but also panels h)-j) show a clear reduction of backscatter area and magnitude. At minute 80 (09:26 UT) it appears that P3 has completely disintegrated, see panel k). In Figure 7 b) we clearly see a strong flow away from the Clyde River radar, where the speed is especially high in the area where P3 starts to break up, indicating that enhanced flow contributes to its rapid decay.

During minute 52 to 62 Clyde River beam 14 overlaps with the RSB FOV, but the intensity measurements are less reliable at large angles from the zenith (low elevation angles) to give a reasonable airglow decay rate. Instead, it is possible to calculate the backscatter half-life from the Clyde River radar. The total decrease in backscatter power for this period is 7.1 dB, corresponding to a half-life of 4.23 minutes. After the stagna-

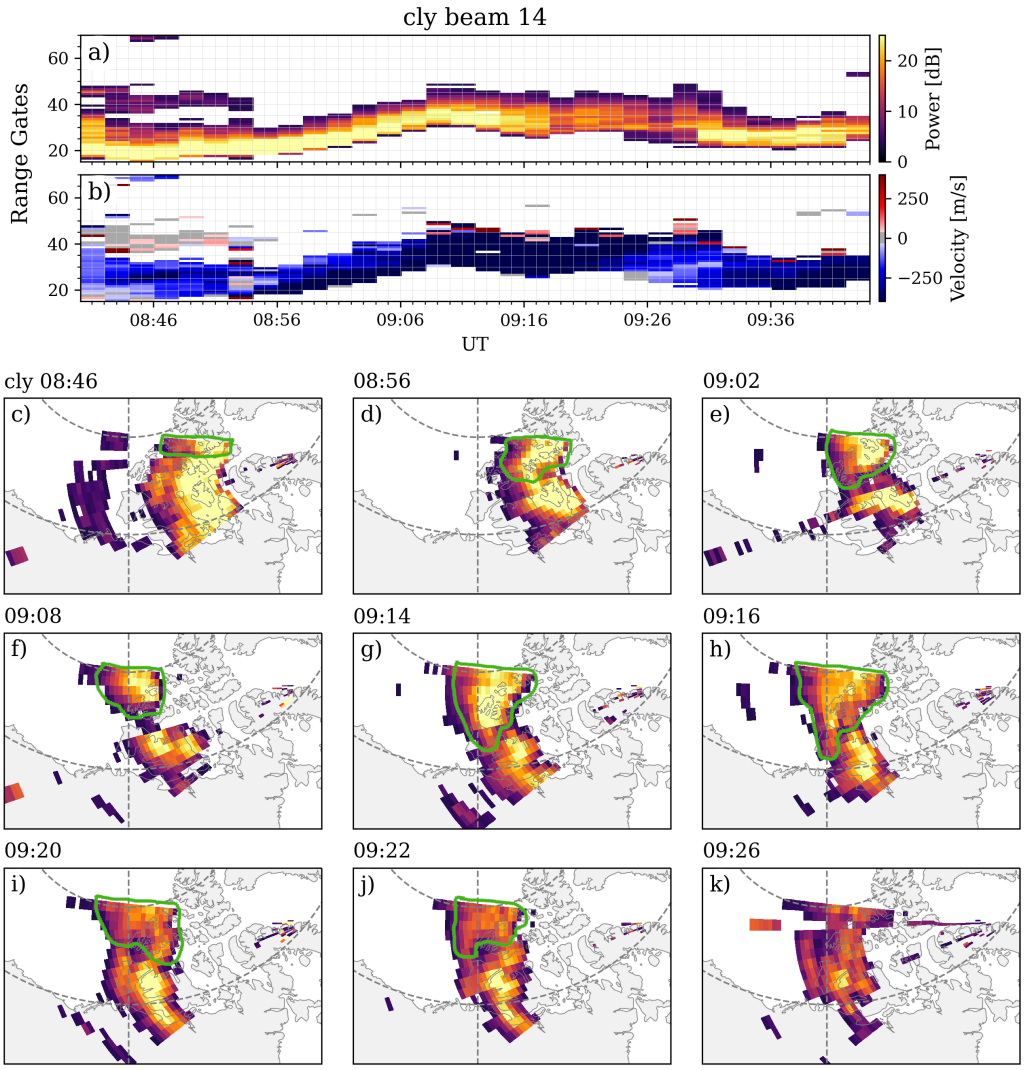

Figure 7. a) backscatter power in beam 14 of the Clyde River SuperDARN radar. b) shows the respective LOS velocity of the beam. c)-k) Clyde River fan plot of backscatter power for selected times. Measurements associated with P3 are outlined in green.

tion, between 68 and 78 minutes, the patch had a total decrease of 16.7 dB, or its half-life decreased to 1.80 minutes.

Figure 8 shows two images from RSB for a) minute 44 (08:50 UT) and b) minute 56 (09:00 UT), where the airglow patch corresponding to P3 has been outlined in blue lines, and the tracking position is shown as a blue star. We chose a location in the airglow patch (76.7407^{o}N, -87.9282 ^{o}W) and found that the new coordinate after 10 minutes was 76.9224^{o}N, -102.3369^{o}W. The airglow patch P3 moved with a velocity of 506.4

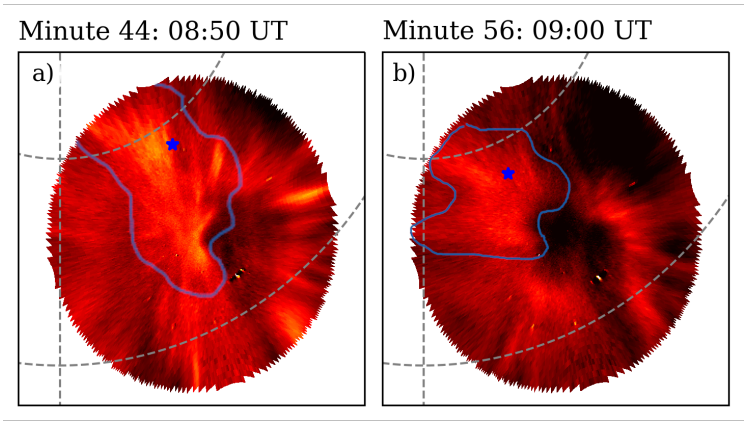

Figure 8. Images from Resolute Bay ASI where the airglow patch 3 is outlined in blue and the tracking position marked with a blue star for the times a) 08:50 UT and b) 09:00 UT.

Table 1. Summary of patch properties

	P1	P2	P3
$t_{release}$ (UT)	07:06	07:18	08:06
$t_{transit}$ (minutes)	104	92	78
t_{exit} (UT)	08:58	09:04	N/A
$n_{initial}(m^{-3})$	1.14×10^{11}	1.48×10^{11}	2.92×10^{11}
$IMF_{initial}$ (x, y, z)	+,+,+	+,+,+	-,+,-
$CA_{initial}$ (degrees)	60	53	170
Airglow decay rate ($\%/minute$)	0.625	0.89	?

m/s. During this 10-minute period it traveled along beam 8 and beam 9 in the Inuvik SuperDARN radar with a mean velocity of 520.24 m/s, while the SuperDARN convection model predicted a mean velocity of 423.97 m/s, giving a relative discrepancy of 18.65% between the model and LOS velocity, and 16.42% between the model and the ASI velocity.

There is a difference between the SuperDARN convection velocity and the Clyde River LOS velocity for minute 60-78, as P3 moves along beam 14. The differences range from 24.7 to 77.8 m/s and the mean absolute error between the model and the LOS velocity is 51.63 m/s. This corresponds to a relative discrepancy of 9.3%.

5 Discussion

This paper presents the evolution of three polar cap patches from their creation on the dayside to their end of life on the nightside, where they either entered the auroral oval or dissipated within the polar cap. The trajectories of the normal-density polar cap patches were determined using SuperDARN convection maps.

The TOI is considered the source of the patches based on TEC data and ESR measurements. The southward IMF before the third patch supports the introduction of Solar EUV plasma into the polar cap, and subsequent formation of the patch due to transient flux transfer events on the dayside magnetopause (Lockwood & Carlson, 1992). During the creation of the two first patches the IMF was northward, which indicates lobe reconnection. Xing et al. (2012) and Wu et al. (2020) showed that a notable number of PMAF-occurrences were in the IMF B_z =[-1,1]nT interval, while 41% and 31%(in the Southern Hemisphere) of PMAFs occurred under northward conditions, respectively. Wu et al. (2020) saw a similar occurrence rate for southward and northward IMF conditions and concluded that PMAFs were more likely to be plasma patches torn away from the auroral oval than direct foot points of reconnecting flux tubes. However, for P1 and P2 the TEC data show a clear transport of lower-latitude plasma towards the pole. Thus, we suggest that the lobe reconnection is the reason that P1 and P2 are less dense than P3, which is released during a PMAF with southward IMF.

5.1 Model Assessment

For the events presented in this work, SuperDARN provided good data coverage over the polar regions, allowing reliable convection patterns to be determined in the regions where the patches were present. In addition, backscatter from the polar cap patches themselves were detected for a large part of their lifetimes, resulting in accurate measurements of velocities and direction. At times when the patches were in regions of sparse SuperDARN data coverage, their trajectory determination relied more heavily on the convection model, which introduces some uncertainties.

Other sources of error in the PCP trajectories are rapid spikes in the IMF clock angle that temporarily distort the convection pattern (Gjerloev et al., 2018), and the chosen release height assumption that determines the initial placement of the patch into the large-scale flow. The clock angle spikes seen right after 08:00 UT in Figure 1 b) were not

of concern for us as the patch trajectories at the time were within an area of good data coverage, and the changes in the convection pattern had no major impact on the trajectories. However, the overall agreement between airglow patches seen in the optical measurements over NYA and RSB and the trajectories created between 06:50 and 08:30 UT are very good, indicating that the method works well with carefully determined initial release location. The events that were selected for the paper showed an especially good fit with the airglow patches.

An average of 583 SuperDARN data points were used in our tracking method, which was successful in tracking average-density polar cap patches, based on the coincident observations of high backscatter power and airglow patches. Comparably, in Oksavik et al. (2010) around 1000 data points contributed to the convection maps when tracking two extreme electron density events. Additionally, the tracking method presented in this paper worked well when there were gaps in the optical data coverage as was seen for P3, i.e., the tracking method connected the PMAF and high-density signatures seen on the dayside with the dissipating backscatter power seen in the Clyde River radar on the nightside. It is reasonable to assume that the tracking method could be used for any density structure in the ionosphere which drifts with the background convection.

Spicher et al. (2015) used SWARM data to measure a PCP at two distinct locations in the polar cap, in the dayside and in the nightside. The SWARM satellites had the initial "pearls-on-a-string"-formation, and the study provides a good example of how PCPs can be tracked over the polar cap outside of using SuperDARN and all-sky cameras. The tracking using SWARM is ideal when the satellite orbit is parallel to the PCP trajectory. Otherwise, it would be difficult to conclude if SWARM were measuring the same patch. Thus, we come back to the need for a general method of tracking PCPs that can tie together several types of instrument observations.

5.2 Transit Times and Intensification in the Nightside Auroral Boundary

P1 and P2 were found to have transit times of 104 and 92 minutes, respectively and both showed a pulsed speed as they traveled through the convection throat on their way to the nightside auroral oval. There are no clear indications that the patch velocities differ from the background convection velocity, as reported by Thomas et al. (2015). How-

ever, the observation of auroral intensification close to the patches exit location at the end of the patches lifetime could indicate a relationship between the auroral intensifications and exiting patches.

At minute 94 for P1 and minute 82 for P2 (08:40 UT) the beginning of an auroral intensification in the nightside auroral oval could be seen in Video 1, followed by subsequent poleward moving, east-west aligned arcs. Poleward boundary intensifications (PBIs) have previously been associated with flow channels and airglow patches (e.g., Zesta et al., 2002; Nishimura et al., 2013, 2014). The fitted velocities vectors seen in Video S1 close to P1 and P2 showed fast flows from 08:22 to 08:46 UT, which could potentially stem from an anti-sunward flow channel that triggered the PBI at 08:40 UT. P1 and P2 used 10 minutes to reach the nightside auroral oval after the first intensification occurred. At minute 96 a decrease in the velocity of P1 was seen, which lasted about 6 minutes. The same type of decrease in the velocity of P2 at minute 84 was seen, lasting around 10 minutes.

Nishimura et al. (2014) suggested that fast flow channels in the lobe that propagated towards the nightside plasma sheet could trigger local nightside reconnection, which appears as PBIs in the optical data. The trajectories of P1 and P2 do not align with the enhanced flow seen in the fitted velocity vectors in their last minutes, and their respective airglow patches are therefore not following the enhanced flow of the first PBI for their entire trajectory. Therefore, neither P1 nor P2 can be said to trigger the PBI. Data from ground magnetometers at Fort Smith and Fort Simpson showed no substorm signatures, suggesting that the PBIs did not trigger any local substorm reconnection on the nightside. Nishimura et al. (2013) reported an airglow patch with embedded polar cap arcs under substorm conditions, which went on to trigger a PBI as it reached the nightside auroral oval. P1 and P2 also appear to be embedded with small-scale aurora-arcs, yet under non-substorm conditions. There are few reports on airglow patches themselves triggering the occurrence of PBIs, but PBIs have been reported during non-substorm conditions previously (Lyons et al., 1999).

In addition to the PBI at 08:42 UT, several other PBIs were seen at 08:54, 09:00, 09:06, and 09:12 UT. Unfortunately, there are no SuperDARN measurements covering the region surrounding the trajectories of P1 and P2 during these times, so it was not possible to confirm that the PBIs were triggered by antisunward flow channels. Nor were

there any 630.0 nm filtered ASI images during this period, so optical confirmation is also not possible. The observation of PBIs could be the ionospheric auroral footprint of bursty bulk flows setting up field aligned currents (Lyons et al., 1999) in the vicinity of P1 and P2 which could lead to nearby velocity shears. In addition, a scattering of most of the virtual particles released close in time to P1 and P2 (see gray dots in Video 1) indicates local velocity shears, which could be explained by P1 and P2 being within the nightside auroral oval.

McWilliams et al. (2000) found that plasma structures had different speeds depending on whether or not they existed within the footprint of an active reconnection region on the dayside. Some structures moved parallel or along the auroral oval boundary. It can therefore be understood that the changing size of the auroral oval itself influences the speed of a drifting plasma structure. In Video 1 the SSUSI model auroral oval boundary expands poleward as both P1 and P2 reach the edge, which would influence the convection flow in its vicinity, since plasma would only be able to pass through an area where reconnection is occurring. Previous studies have found that the auroral oval expands towards drifting airglow patches during active magnetic reconnection periods (e.g., Lorentzen et al., 2004). From the results presented in this paper it is reasonable to assume that reconnection occurs in the vicinity of P1 and P2 as they enter the auroral oval, however on such a scale that the magnetic disturbances occurring at $\sim$ 250km altitude are too small to propagate down to the ground magnetometer.

5.3 Airglow Decay Rates

The average airglow decay rate of P1 and P2 were found to be $\approx 0.6\%$ and $\approx 0.9\%$ per minute, respectively. Both P1 and P2 traversed the RSB FOV in a time-interval where small-scale auroral-arcs were present, and the decay rates could therefore include contribution from aurora. P1 appeared to be more co-located with the small-scale auroral-arcs than P2, but were consistently so, thus the contribution from the aurora would not change much for the transit. Neither of the decay rates showed any significant correlation to patch velocity, which were pulsed during the respective times. Hosokawa et al. (2011) investigated the density and airglow loss rate of an airglow patch that had stagnated over the RSB FOV and found that after stagnation, the airglow decreased rapidly within a 20-minutes period, before it slowed. Since P1 and P2 were still in motion the

decay rates found in this paper are not directly comparable, however it does support the notion that a patch in motion has a slower decay than a stationary patch.

The highest relative intensity of P2 occurred at minute 58 before it decreased by 16% over the next 18 minutes. At this time P2 moved in magnetic latitude from 83.6 ^{o}N to 79.5^{o}N. The decrease in magnetic latitude indicates that at least a portion of the airglow decay came from the altitude change of the airglow patch, since there is a downward component of the ExB-drift of the patch as it travels away from the magnetic pole, which is associated with a decrease in luminosity (Perry et al., 2013). Hosokawa et al. (2011) also showed that as the airglow patch traveled over the polar cap the peak airglow height of the patch increased, due to the recombination in the bottom layers of the airglow patch. That means that the mapping height of 230 km, which is used in this paper, may not be optimal despite a downward motion of the patch. However, we have no easy method to decide which altitude the patch existed in.

If we had not applied the image process described in Section 2.3, no significant decrease in luminosity would be seen for P1 and P2 in the ASI images, which is not surprising since both the background and the aurora contaminated the measurements. P3 had a slow decrease in luminosity, without the contamination of aurora as mentioned in Section 4.3. It is also worth mentioning that a big drop in luminosity occurred at minute 68 after the stagnation of P3, which corresponds perfectly to the initial breakup seen in Clyde River backscatter power, Figure 7 a). However, the camera elevation angles were all less than 20^o, which means the result should not be over-interpreted due to unfavorable observing geometry. Even by implementing the method used in Kubota et al. (2014) to correct for low elevation angles, there is still no obvious decay in the airglow for P3, only a fluctuating emission intensity, while the patch is still in motion.

5.4 The Complete Dissipation of Patch 3

P3 was created after a longer period of Southward IMF where ESR measured more dense plasma compared to P1 and P2, see Figure 1 a). P3's transit also differed from P1 and P2 as it never reached the nightside auroral oval, but instead underwent a complete decay within the polar cap.

Initially, P3 traveled within the convection throat with a steady velocity around 500 m/s for the first 20 minutes, before a rapid increase in velocity reaching 1000 m/s

within the next 30 minutes. Considering Figure 1 a) a period of ≈ 40 minutes of southward IMF is seen, starting a few minutes after 08:00 UT, which could result in increased dayside reconnection. The IMF was southward for P3 (northward for P1 and P2) and could explain the intense PMAF, and thus high flux transfer. This rapid reconnection rate could also be responsible for the enhanced flow seen in the convection throat (Ren et al., 2020), and thus the increase in the P3 velocity before minute 30.

Later P3 moved within the LOS of beam 14 of Clyde River for almost 40 minutes before it appeared to completely disintegrate. The observation provides a unique insight into what determines the breakup of a polar cap patch. No significant indications in the solar wind measurements were present. However, convection maps with their fitted velocities vectors indicate that P3 was close to a region of enhanced flows at minute 48 (08:54 UT). In the individual radars Clyde River, Rankin Inlet and Inuvik, the enhanced flows are sometimes structured as flow channels, but at other times they have a wider horizontal extent. As P3 entered the region of enhanced flow, the trajectory changed from moving straight towards magnetic midnight to a duskward direction.

In the Kaktovik magnetometer (not shown), a tail loading phase starts at around 08:50 UT and shows a steady decreasing depression down to -100nT until 09:34 UT before the onset of a -200nT substorm occurs. In Figure 1 a) a turn from northward to southward IMF can be seen just before 08:00 UT, which could initiate the loading phase. One theory is that the loading phase could set up bursty bulk flows creating disturbances in the nightside convection which could lead to the enhanced flows and that these flows themselves could lead to the decay of P3. Rankin Inlet velocity fan plots indicate that there are regions in the vicinity of the P3 transit with flows in different directions which would lead to strong shears in the convection. Hosokawa et al. (2010) found that a polar cap patch with internal structures could be restructured into several smaller polar cap patches because of shears in the background convection and suggested it could also lead to dissipation of polar cap patches.

The gradient drift instability (GDI) has previously been seen to be relatively large in the trailing edge of a polar cap patch (Milan et al., 2002) and is also considered an important internal structuring mechanism of an airglow patch. As P3 underwent a rotation during its transit, this would indicate a new trailing edge with respect to the background convection. Assuming the GDI in the old trailing edge did not immediately sta-

bilize, a new trailing edge would provide a larger portion of the polar cap patch border to be available for strong GDI, which would be free to propagate inwards and could potentially accelerate the decay of P3.

Based on Clyde River backscatter power measurements in Figure 7 a), P3 stagnates at minute 62 (09:08 UT), and this stagnation appears to be a key step of the transit which results in a complete decay of the patch. Fan plots show a rapid change in the Clyde River and Rankin Inlet LOS velocities, and the introduction of the enhanced flows mentioned above would create a big relative velocity difference in the ion drift and the neutral wind. This difference leads to increased frictional heating, which again leads to faster recombination, depleting the patch. The neutral wind response time has been reported to be both altitude dependent (from 45 minutes at 400km to 1.5 hours at 200km), as well as magnetic activity dependent (from 0.5 to 6.5 hours during active to quiet periods) (Kosch et al., 2001; Deng et al., 2009). Billett et al. (2019) showed that the neutral wind response time had a significant effect on the ion-neutral coupling, and thus energy transfer.

Hosokawa et al. (2011) studied the complete decay of an airglow patch during strong northward IMF conditions, and Q. H. Zhang et al. (2013) used TEC data to study the formation of a polar cap patch and its subsequent decay during geomagnetic storm conditions and week northward IMF. Q. H. Zhang et al. (2013) saw that after the initial formation of the PCP the IMF turned from strong southward to weak northward conditions, which caused the trajectory of the patch to stagnate on the dayside, before it dissipated completely. The dissipation of the PCP was suggested to be due to the effects stemming from the opposite directions of the ion drift and the neutral wind after the change in the IMF.

After the change of direction of P3 at minute 50 it took 12 minutes for the patch to stagnate, and 28 minutes to dissipate completely. This is within the reported neutral wind response time. Both Q. H. Zhang et al. (2013) and Hosokawa et al. (2011) present a PCP stagnating before complete dissipation. These three observations of complete decay of a PCP under different IMF and ionospheric conditions; weak northward with extreme density patch (≈35 TECU) for Q. H. Zhang et al. (2013), strong northward (≈4nT) in Hosokawa et al. (2011), and southward (≈2nT) for minute 62 of P3, of ordinary electron density, suggest that the sudden change in the trajectory leads to a stagnation of

the polar cap patch. Hence, stagnation becomes a key occurrence in deciding whether or not a polar cap patch would be able to exit the auroral oval on the nightside.

10 minutes before the stagnation, the backscatter power had a half-life of 4.23 minutes. At minute 68 (09:14 UT) a rapid decay of Clyde River backscatter power is seen in Figure 7 b) and the half-life decreased to 1.80 minutes (minutes 68-74). Thus, the backscatter power shows a similar evolution to the airglow of P1 and P2. As mentioned previously, there was a big drop in the emission intensity of the RSB images as well, which occurred simultaneous to the rapid decay between minute 68 and 74, indicating that the drop in emission intensity is not solely due to the observing geometry of low ASI elevation angles, i.e., below 20^o.

Due to the lack of incoherent scatter radar measurements in the vicinity of P3 at minute 52 (78.42^oN, 96.923^oE) no relationship between electron density decay and backscatter power decay can be made. Instead, we compare the theoretical electron density decay rate, and therefore 630.0 nm emission decay rate, following the method described in Hosokawa et al. (2011). The MSIS-E-90 Atmosphere model (Hedin, 1991) model gives the following values for neutral temperature, $[N_2]$ and $[O_2]$ at 280km: 975.2K, 2.108E8 cm^{-3}, and 1.346E7 cm^{-3}. This produces a half-life of $\approx$34 minutes, which is substantially longer than the backscatter half-life of 4.23 minutes. This suggests that exponential decay, where we assume no production and neglect the divergence in the ion drift's influence on the decay rate, is not suitable for a PCP still in motion. Future investigations using incoherent scatter radar measurements at various stages of the PCP's lifetime is needed for a complete description of the decay rate. Nevertheless, the discussion indicates that the decay rate is not constant throughout the lifetime of a PCP.

In addition to velocity shears, GDI instabilities and frictional heating, gravity waves and vertical winds have been known to influence the 630.0 nm emission intensity in airglow patches (Valladares et al., 2015). Gravity waves and vertical winds could potentially explain the fluctuating intensity that was observed for P3 before the rotation occurred, which supports a variable decay rate of a polar cap in motion.

The velocity measurements from Clyde River made it possible to compare the SuperDARN LOS and convection model velocity during the P3 transit. In Figure 6 a) during minute 60 and 78 the markers for Clyde River LOS velocity show a higher velocity than the convection model. The relative discrepancy between the Clyde River LOS and

model velocity was found to be 9.3% or a mean absolute error of 51.6 m/s. This suggests an underestimation of the SuperDARN model convection velocity. Two possible contributors to this underestimation are 1) the SuperDARN velocity determination does not account for the ionospheric refractive index (Gillies et al., 2009), and 2) the SuperDARN analysis software performs median filtering and weighted averaging procedures on the LOS velocity measurements before determining the convection pattern.

An attempt at comparing the airglow patch velocity, the P3 transit velocity, and the Inuvik LOS velocity was done to see if the P3 transit velocity also showed an underestimation compared to the LOS velocity. Between minute 44 and 54 the airglow patch moved at 506.4 m/s, and the Inuvik Radar had a mean velocity of 520.24 m/s, while the convection model velocity was 423.97 m/s giving a relative discrepancy of 16.42 % and 18.65% for ASI velocity and Inuvik radar, respectively. This indicates that the SuperDARN convection velocity can be underestimated by almost 20% in some cases and is supported by previous reports of the underestimation (Ponomarenko et al., 2009; Gillies et al., 2009, 2010; Koustov et al., 2016).

6 Conclusion

In this paper we have investigated three polar cap patch transits and their change in velocity, luminosity, and decay rates. The polar cap patches were of an average density and were created on the dayside from solar EUV dense-plasma and PMAFs, before they propagated over the polar cap. Two of the patches reached the nightside auroral oval, while the third decayed completely within the polar cap. We summarize our findings in the order they were discussed:

1. Given strong IMF By, which favors strong backscatter over the Canadian/Alaskan sector, the tracking of high-density plasma volumes in the ionosphere unites observations from different instruments that are not co-located.
2. Patches 1 and 2 transit in the convection throat and entered the nightside auroral oval. Their transit times were 104 and 92 minutes, respectively. In the last few minutes, of both patches, a decrease in velocity was seen as PBIs occurred in the vicinity of their exit point in the nightside polar cap.
3. Relative airglow decay rates were ≈0.6% and ≈0.9% per minute for patch 1 and patch 2, respectively.

4. Patch 3 dissipated completely after 78 minutes. A change in direction is observed due to enhanced flows, and the patch had a backscatter power half-life of 4.23 minutes. At minute 62 the patch appears to stagnate, and shortly after the half-life has decreased to 1.80 minutes, likely due to the increased frictional heating stemming from a relative velocity difference in ion drift and neutral wind. 16 minutes after stagnation, and 28 minutes after the change in transit direction, patch 3 completely dissipated.
5. A polar cap patch still in motion appears to have a variable decay rate.
6. The stagnation, and increased frictional heating (higher recombination rates), is theorized to be a major determinant to whether a polar cap patch will reach the nightside auroral oval or not.
7. The SuperDARN convection model underestimated the velocity with 18.65% and 16.42% compared to the Inuvik LOS velocity and RSB ASI airglow patch velocity.

7 Open Research

Data Availability Statement

SuperDARN RAWACF data can be collected from the FRDR database (`https://doi.org/10.20383/102.0448`) and has been processed and analyzed using RST (`https://doi.org/10.5281/ZENODO.5156752`) and pydarn `https://doi.org/10.5281/zenodo.5762322`)(SuperDARN Data Analysis Working Group et al., 2021). The Kp-index was provided by GFZ German Research Centre for Geosciences (Matzka, Stolle, et al., 2021; Matzka, Bronkalla, et al., 2021). The EISCAT data and DMSP SSIES data are available through the CEDAR Madrigal database (`http://cedar.openmadrigal.org/`) and the solar wind IMF data from ACE can be collected from `https://cdaweb.gsfc.nasa.gov/index.html`. The ASI data from UiO can be collected from `http://tid.uio.no/plasma/aurora/` and THEMIS images are available from `http://themis.igpp.ucla.edu/data_retrieval.shtml`. The OMTI all-sky camera images are available from `https://ergsc.isee.nagoya-u.ac.jp/index.shtml.en`. The DMSP SSUSI data (product version V0105) was collected from `https://ssusi.jhuapl.edu/data_products`. MSIS values were collected from `https://ccmc.gsfc.nasa.gov/modelweb/models/msis_vitmo.php`.

Acknowledgments

The Birkeland Center for Space Science is funded by the Research Council of Norway/CoE under contract 223252/F50. We thank the support from the ISSI/ISSI-BJ for the international team on "Multi-Scale Magnetosphere-Ionosphere-Thermosphere Interaction." The authors acknowledge the use of SuperDARN data. SuperDARN is a collection of radars funded by national scientific funding agencies of Australia, Canada, China, France, Italy, Japan, Norway, South Africa, United Kingdom, and the United States of America. EISCAT is an international association supported by research organizations in China (CRIRP), Finland (SA), Japan (NIPR and ISEE), Norway (NFR), Sweden (VR), and the United Kingdom (UKRI). The Norwegian participation in EISCAT and EISCAT_3D is funded by the Research Council of Norway through research infrastructure grant 245683. We acknowledge NASA contract NAS5-02099 and V. Angelopoulos for use of data from the THEMIS Mission. Specifically, S. Mende and E. Donovan for use of the ASI data, the CSA for logistical support in fielding and data retrieval from the GBO stations, and NSF for support of GIMNAST through grant AGS-1004736. The optical observation at Resolute Bay was financially supported by the JSPS (Japan Society for Promotion of Science) Grants-in-Aid for Scientific Research (16H06286, 26302006). We would also like to thank the late Dr. Patricia Doherty and Dr. Marc Hairston for the use of the DMSP SSIES data. T. K. Yeoman was supported by STFC Grant ST/W00089X/1 and NERC Grant NE/V000748/1.

References

Billett, D. D., Wild, J. A., Grocott, A., Aruliah, A. L., Ronksley, A. M., Walach, M. T., & Lester, M. (2019, 8). Spatially Resolved Neutral Wind Response Times During High Geomagnetic Activity Above Svalbard. *Journal of Geophysical Research: Space Physics*, *124*(8), 6950–6960. doi: 10.1029/2019JA026627

Carlson, H. C. (2012). Sharpening our thinking about polar cap ionospheric patch morphology, research, and mitigation techniques. *Radio Sci.*, *47*(3). doi: 10.1029/2011RS004946

Chisham, G., Lester, A. M., Milan, A. S. E., Freeman, A. M. P., Bristow, A. W. A., Grocott, A. A., ... Sato, N. (2007, 5). A decade of the Super Dual Auroral Radar Network (SuperDARN): scientific achievements, new techniques

and future directions. *Surveys in Geophysics 2007 28:1*, *28*(1), 33–109. doi: 10.1007/S10712-007-9017-8

Crowley, G. (1996). Critical review of ionospheric patches and blobs. *Review of Radio Science 1993–1996*, 619–648.

Deng, Y., Lu, G., Kwak, Y. S., Sutton, E., Forbes, J., & Solomon, S. (2009, 7). Reversed ionospheric convections during the November 2004 storm: Impact on the upper atmosphere. *Journal of Geophysical Research: Space Physics*, *114*(A7), 7313. doi: 10.1029/2008JA013793

Foster, J. C., Coster, A. J., Erickson, P. J., Holt, J. M., Lind, F. D., Rideout, W., ... Rich, F. J. (2005, 9). Multiradar observations of the polar tongue of ionization. *Journal of Geophysical Research: Space Physics*, *110*(A9), 9–31. doi: 10.1029/2004JA010928

Gillies, R. G., Hussey, G. C., Sofko, G. J., McWilliams, K. A., Fiori, R. A., Ponomarenko, P., & St.-Maurice, J. P. (2009, 7). Improvement of SuperDARN velocity measurements by estimating the index of refraction in the scattering region using interferometry. *Journal of Geophysical Research: Space Physics*, *114*(A7), 7305. doi: 10.1029/2008JA013967

Gillies, R. G., Hussey, G. C., Sofko, G. J., Wright, D. M., & Davies, J. A. (2010, 6). A comparison of EISCAT and SuperDARN F-region measurements with consideration of the refractive index in the scattering volume. *Journal of Geophysical Research: Space Physics*, *115*(A6). doi: 10.1029/2009JA014694

Gjerloev, J. W., Waters, C. L., & Barnes, R. J. (2018, 4). Deriving Global Convection Maps From SuperDARN Measurements. *Journal of Geophysical Research: Space Physics*, *123*(4), 2902–2915. doi: 10.1002/2017JA024543

Goodwin, L. V., Iserhienrhien, B., Miles, D. M., Patra, S., Van Der Meeren, C., Buchert, S. C., ... Moen, J. (2015, 2). Swarm in situ observations of F region polar cap patches created by cusp precipitation. *Geophysical Research Letters*, *42*(4), 996–1003. doi: 10.1002/2014GL062610

Greenwald, R. A., Baker, K. B., Dudeney, J. R., Pinnock, M., Jones, T. B., Thomas, E. C., ... Yamagishi, H. (1995, 2). DARN/SuperDARN. *Space Science Reviews 1995 71:1*, *71*(1), 761–796. doi: 10.1007/BF00751350

Hays, P. B., Rusch, D. W., Roble, R. G., & Walker, J. C. G. (1978). The O I (6300 Å) airglow. *Reviews of Geophysics*, *16*(2), 225–232. doi:

10.1029/RG016I002P00225

Hedin, A. E. (1991, 2). Extension of the MSIS Thermosphere Model into the middle and lower atmosphere. *Journal of Geophysical Research: Space Physics*, *96*(A2), 1159–1172. doi: 10.1029/90JA02125

Hosokawa, K., Kashimoto, T., Suzuki, S., Shiokawa, K., Otsuka, Y., & Ogawa, T. (2009, 4). Motion of polar cap patches: A statistical study with all-sky airglow imager at Resolute Bay, Canada. *Journal of Geophysical Research: Space Physics*, *114*(A4). doi: 10.1029/2008JA014020

Hosokawa, K., Moen, J. I., Shiokawa, K., & Otsuka, Y. (2011). Decay of polar cap patch. *Journal of Geophysical Research: Space Physics*, *116*(5). doi: 10.1029/2010JA016297

Hosokawa, K., St-Maurice, J. P., Sofko, G. J., Shiokawa, K., Otsuka, Y., & Ogawa, T. (2010, 1). Reorganization of polar cap patches through shears in the background plasma convection. *Journal of Geophysical Research: Space Physics*, *115*(A1), 1303. doi: 10.1029/2009JA014599

Hosokawa, K., Taguchi, S., & Ogawa, Y. (2016, 4). Edge of polar cap patches. *Journal of Geophysical Research: Space Physics*, *121*(4), 3410–3420. doi: 10.1002/2015JA021960

Hwang, K. J., Nishimura, Y., Coster, A. J., Gillies, R. G., Fear, R. C., Fuselier, S. A., ... Clausen, L. B. (2020, 6). Sequential Observations of Flux Transfer Events, Poleward-Moving Auroral Forms, and Polar Cap Patches. *Journal of Geophysical Research: Space Physics*, *125*(6), e2019JA027674. doi: 10.1029/2019JA027674

Ivarsen, M. F., Jin, Y., Spicher, A., Miloch, W., & Clausen, L. B. (2021, 2). The Lifetimes of Plasma Structures at High Latitudes. *Journal of Geophysical Research: Space Physics*, *126*(2), e2020JA028117. doi: 10.1029/2020JA028117

Jin, Y., Moen, J. I., & Miloch, W. J. (2014). GPS scintillation effects associated with polar cap patches and substorm auroral activity: direct comparison. *Journal of Space Weather and Space Climate*, *4*, A23. doi: 10.1051/SWSC/2014019

Kosch, M. J., Cierpka, K., Rietveld, M. T., Hagfors, T., & Schlegel, K. (2001, 4). High-latitude ground-based observations of the thermospheric ion-drag time constant. *Geophysical Research Letters*, *28*(7), 1395–1398. doi:

10.1029/2000GL012380

Koustov, A. V., Lavoie, D. B., & Varney, R. H. (2016, 11). On the consistency of the SuperDARN radar velocity and E × B plasma drift. *Radio Science*, *51*(11), 1792–1805. doi: 10.1002/2016RS006134

Kubota, M., Fukunishi, H., & Okano, S. (2014, 6). Characteristics of medium- and large-scale TIDs over Japan derived from OI 630-nm nightglow observation. *Earth, Planets and Space 2001 53:7*, *53*(7), 741–751. doi: 10.1186/BF03352402

Lockwood, M., & Carlson, H. C. (1992, 9). Production of polar cap electron density patches by transient magnetopause reconnection. *Geophysical Research Letters*, *19*(17), 1731–1734. doi: 10.1029/92GL01993

Lockwood, M., Davies, J. A., Moen, J., van Eyken, A. P., Oksavik, K., McCrea, I. W., & Lester, M. (2005, 12). Motion of the dayside polar cap boundary during substorm cycles: II. Generation of poleward-moving events and polar cap patches by pulses in the magnetopause reconnection rate. *Annales Geophysicae*, *23*(11), 3513–3532. doi: 10.5194/ANGEO-23-3513-2005

Lorentzen, D. A., Moen, J., Oksavik, K., Sigernes, F., Saito, Y., & Johnsen, M. G. (2010). In situ measurement of a newly created polar cap patch. *Journal of Geophysical Research: Space Physics*, *115*(12), 1–11. doi: 10.1029/2010JA015710

Lorentzen, D. A., Shumilov, N., & Moen, J. (2004, 1). Drifting airglow patches in relation to tail reconnection. *Geophysical Research Letters*, *31*(2). doi: 10.1029/2003GL017785

Lyons, L. R., Nagai, T., Blanchard, G. T., Samson, J. C., Yamamoto, T., Mukai, T., ... Kokubun, S. (1999, 3). Association between Geotail plasma flows and auroral poleward boundary intensifications observed by CANOPUS photometers. *Journal of Geophysical Research: Space Physics*, *104*(A3), 4485–4500. doi: 10.1029/1998JA900140

Matzka, J., Bronkalla, O., Tornow, K., Elger, K., & Stolle, C. (2021). *Geomagnetic Kp index. V. 1.0.* FZ Data Services. doi: 10.5880/Kp.0001

Matzka, J., Stolle, C., Yamazaki, Y., Bronkalla, O., & Morschhauser, A. (2021, 5). The Geomagnetic Kp Index and Derived Indices of Geomagnetic Activity. *Space Weather*, *19*(5). doi: 10.1029/2020SW002641

McWilliams, K. A., Yeoman, T. K., & Cowley, S. W. H. (2000, 12). Two-dimensional electric field measurements in the ionospheric footprint of a flux transfer event. *Annales Geophysicae*, *18*(12), 1584–1598. doi: 10.1007/S00585-001-1584-2

Milan, S. E., Lester, M., & Yeoman, T. K. (2002). HF radar polar patch formation revisited: Summer and winter variations in dayside plasma structuring. *Annales Geophysicae*, *20*(4), 487–499. doi: 10.5194/ANGEO-20-487-2002

Moen, J., Oksavik, K., Alfonsi, L., Daabakk, Y., Romano, V., & Spogli, L. (2013). Space weather challenges of the polar cap ionosphere. *Journal of Space Weather and Space Climate*, *3*, A02. doi: 10.1051/SWSC/2013025

Nishimura, Y., Lyons, L. R., Shiokawa, K., Angelopoulos, V., Donovan, E. F., & Mende, S. B. (2013, 5). Substorm onset and expansion phase intensification precursors seen in polar cap patches and arcs. *Journal of Geophysical Research: Space Physics*, *118*(5), 2034–2042. doi: 10.1002/JGRA.50279

Nishimura, Y., Lyons, L. R., Zou, Y., Oksavik, K., Moen, J. I., Clausen, L. B., ... Lester, M. (2014, 6). Day-night coupling by a localized flow channel visualized by polar cap patch propagation. *Geophysical Research Letters*, *41*(11), 3701–3709. doi: 10.1002/2014GL060301

Nishitani, N., Ruohoniemi, J. M., Lester, M., Baker, J. B. H., Koustov, A. V., Shepherd, S. G., ... Kikuchi, T. (2019, 3). Review of the accomplishments of mid-latitude Super Dual Auroral Radar Network (SuperDARN) HF radars. *Progress in Earth and Planetary Science*, *6*(1), 1–57. doi: 10.1186/s40645-019-0270-5

Oksavik, K., Barth, V. L., Moen, J., & Lester, M. (2010, 12). On the entry and transit of high-density plasma across the polar cap. *Journal of Geophysical Research: Space Physics*, *115*(A12). doi: 10.1029/2010JA015817

Oksavik, K., Ruohoniemi, J. M., Greenwald, R. A., Baker, J. B. H., Moen, J., Carlson, H. C., ... Lester, M. (2006). Observations of isolated polar cap patches by the European Incoherent Scatter (EISCAT) Svalbard and Super Dual Auroral Radar Network (SuperDARN) Finland radars. *Journal of Geophysical Research: Space Physics*, *111*(A5). doi: 10.1029/2005JA011400

Oksavik, K., Van Der Meeren, C., Lorentzen, D. A., Baddeley, L. J., & Moen, J. (2015, 10). Scintillation and loss of signal lock from poleward moving auroral

807 forms in the cusp ionosphere. *Journal of Geophysical Research: Space Physics*,
808 *120*(10), 9161–9175. doi: 10.1002/2015JA021528

809 Paxton, L. J., & Meng, C.-I. (1999). Auroral Imaging and Space-Based Optical Re-
810 mote Sensing. *Johns Hopkins APL technical digest*, *20*(4), 556–569.

811 Paxton, L. J., Morrison, D., Zhang, Y., Kil, H., Wolven, B., Ogorzalek, B. S., ...
812 Meng, C.-I. (2002, 1). Validation of remote sensing products produced by the
813 Special Sensor Ultraviolet Scanning Imager (SSUSI): a far UV-imaging spec-
814 trograph on DMSP F-16. *https://doi.org/10.1117/12.454268*, *4485*, 338–348.
815 doi: 10.1117/12.454268

816 Paxton, L. J., & Zhang, Y. (2016, 11). Far Ultraviolet Imaging of the Aurora. *Space*
817 *Weather Fundamentals*, 213–244. doi: 10.1201/9781315368474-14

818 Perry, G. W., St.-Maurice, J. P., & Hosokawa, K. (2013, 11). The interconnection
819 between cross–polar cap convection and the luminosity of polar cap patches.
820 *Journal of Geophysical Research: Space Physics*, *118*(11), 7306–7315. doi:
821 10.1002/2013JA019196

822 Ponomarenko, P. V., St-Maurice, J. P., Waters, C. L., Gillies, R. G., & Koustov,
823 A. V. (2009, 11). Refractive index effects on the scatter volume location and
824 Doppler velocity estimates of ionospheric HF backscatter echoes. *Annales*
825 *Geophysicae*, *27*(11), 4207–4219. doi: 10.5194/ANGEO-27-4207-2009

826 Ren, J., Zou, S., Kendall, E., Coster, A., Sterne, K., & Ruohoniemi, M. (2020, 4).
827 Direct Observations of a Polar Cap Patch Formation Associated With Day-
828 side Reconnection Driven Fast Flow. *Journal of Geophysical Research: Space*
829 *Physics*, *125*(4), e2019JA027745. doi: 10.1029/2019JA027745

830 Rodger, A. S., Pinnock, M., Dudeney, J. R., Baker, K. B., & Greenwald, R. A.
831 (1994, 4). A new mechanism for polar patch formation. *Journal of Geophysical*
832 *Research: Space Physics*, *99*(A4), 6425–6436. doi: 10.1029/93JA01501

833 Ruohoniemi, J. M., & Baker, K. B. (1998, 9). Large-scale imaging of high-latitude
834 convection with Super Dual Auroral Radar Network HF radar observations.
835 *Journal of Geophysical Research: Space Physics*, *103*(A9), 20797–20811. doi:
836 10.1029/98JA01288

837 Sandholt, P. E., Deehr, C. S., Egeland, A., Lybekk, B., Viereck, R., & Romick,
838 G. J. (1986, 9). Signatures in the dayside aurora of plasma transfer from the
839 magnetosheath. *Journal of Geophysical Research: Space Physics*, *91*(A9),

10063–10079. doi: 10.1029/JA091IA09P10063

Sandholt, P. E., Farrugia, C. J., & Denig, W. F. (2004). Detailed dayside auroral morphology as a function of local time for southeast IMF orientation: Implications for solar wind-magnetosphere coupling. *Annales Geophysicae*, *22*(10), 3537–3560. doi: 10.5194/ANGEO-22-3537-2004

Sandholt, P. E., Farrugia, C. J., Moen, J., & Cowley, S. W. H. (1998). Dayside auroral configurations: Responses to southward and northward rotations of the interplanetary magnetic field. *Journal of Geophysical Research: Space Physics*, *103*(A9), 20279–20295. doi: 10.1029/98JA01541

Shiokawa, K., Katoh, Y., Satoh, M., Ejiri, M. K., Ogawa, T., Nakamura, T., ... Wiens, R. H. (1999). Development of optical mesosphere thermosphere imagers (OMTI). *Earth, Planets and Space*, *51*(7), 887–896.

Shiokawa, K., Otsuka, Y., & Ogawa, T. (2009, 5). Propagation characteristics of nighttime mesospheric and thermospheric waves observed by optical mesosphere thermosphere imagers at middle and low latitudes. *Earth, Planets and Space*, *61*(4), 479–491. doi: 10.1186/BF03353165

Southwood, D. J. (1987, 4). The ionospheric signature of flux transfer events. *Journal of Geophysical Research: Space Physics*, *92*(A4), 3207–3213. doi: 10.1029/JA092IA04P03207

Spicher, A., Cameron, T., Grono, E. M., Yakymenko, K. N., Buchert, S. C., Clausen, L. B., ... Moen, J. I. (2015, 1). Observation of polar cap patches and calculation of gradient drift instability growth times: A Swarm case study. *Geophysical Research Letters*, *42*(2), 201–206. doi: 10.1002/2014GL062590

SuperDARN Data Analysis Working Group., Schmidt, M., Bland, E., Thomas, E., Burrell, A., Coco, I., ... Walach, M.-T. (2021, 8). *SuperDARN/rst: RST 4.6.* Retrieved from `https://zenodo.org/record/5156752` doi: 10.5281/ZENODO.5156752

SuperDARN Data Analysis Working Group, Schmidt, M., Tholley, F., Martin, C., Billett, D., Bland, E., ... Roberston, C. (2021, 12). *SuperDARN/pydarn: pyDARN v2.2.1.* Retrieved from `https://zenodo.org/record/5762322` doi: 10.5281/ZENODO.5762322

Thomas, E. G., Hosokawa, K., Sakai, J., Baker, J. B. H., Ruohoniemi, J. M., Taguchi, S., ... McWilliams, K. A. (2015, 9). Multi-instrument, high-

resolution imaging of polar cap patch transportation. *Radio Science*, *50*(9), 904–915. doi: 10.1002/2015RS005672

Valladares, C. E., Pedersen, T., & Sheehan, R. (2015, 9). Polar cap patches observed during the magnetic storm of November 2003: Observations and modeling. *Annales Geophysicae*, *33*(9), 1117–1133. doi: 10.5194/angeo-33-1117-2015

Van Der Meeren, C., Oksavik, K., Lorentzen, D., Moen, J. I., & Romano, V. (2014, 10). GPS scintillation and irregularities at the front of an ionization tongue in the nightside polar ionosphere. *Journal of Geophysical Research: Space Physics*, *119*(10), 8624–8636. doi: 10.1002/2014JA020114

Walker, I. K., Moen, J., Kersley, L., & Lorentzen, D. A. (1999). On the possible role of cusp/cleft precipitation in the formation of polar-cap patches. *Annales Geophysicae 1999 17:10*, *17*(10), 1298–1305. doi: 10.1007/S00585-999-1298-4

Wannberg, G., Wolf, I., Vanhainen, L. G., Koskenniemi, K., Röttger, J., Postila, M., ... Huuskonen, A. (1997). The EISCAT Svalbard radar: A case study in modern incoherent scatter radar system design. *Radio Science*, *32*(6), 2283–2307. doi: 10.1029/97RS01803

Weber, E. J., Buchau, J., Moore, J. G., Sharber, J. R., Livingston, R. C., Winningham, J. D., & Reinisch, B. W. (1984, 3). F layer ionization patches in the polar cap. *Journal of Geophysical Research: Space Physics*, *89*(A3), 1683–1694. doi: 10.1029/JA089IA03P01683

Wu, Y. J. J., Mende, S. B., & Frey, H. U. (2020, 6). Simultaneous Observations of Poleward-Moving Auroral Forms at the Equatorward and Poleward Boundaries of the Auroral Oval in Antarctica. *Journal of Geophysical Research: Space Physics*, *125*(6), e2019JA027646. doi: 10.1029/2019JA027646

Xing, Z. Y., Yang, H. G., Han, D. S., Wu, Z. S., Hu, Z. J., Zhang, Q. H., ... Huang, D. H. (2012, 9). Poleward moving auroral forms (PMAFs) observed at the Yellow River Station: A statistical study of its dependence on the solar wind conditions. *Journal of Atmospheric and Solar-Terrestrial Physics*, *86*, 25–33. doi: 10.1016/J.JASTP.2012.06.004

Zesta, E., Donovan, E., Lyons, L., Enno, G., Murphree, J. S., & Cogger, L. (2002, 11). Two-dimensional structure of auroral poleward boundary intensifications. *Journal of Geophysical Research: Space Physics*, *107*(A11), 6–1. doi: 10.1029/2001JA000260

Zhang, Q. H., Zhang, B. C., Lockwood, M., Hu, H. Q., Moen, J., Ruohoniemi, J. M., ... Baker, J. B. (2013, 3). Direct observations of the evolution of polar cap ionization patches. *Science*, *340*(6127), 1597–1600. doi: 10.1126/science.1231487

Zhang, Y., & Paxton, L. J. (2008, 6). An empirical Kp-dependent global auroral model based on TIMED/GUVI FUV data. *Journal of Atmospheric and Solar-Terrestrial Physics*, *70*(8-9), 1231–1242. doi: 10.1016/J.JASTP.2008.03.008

Zou, Y., Nishimura, Y., Lyons, L. R., Shiokawa, K., Donovan, E. F., Ruohoniemi, J. M., ... Nishitani, N. (2015). Localized polar cap flow enhancement tracing using airglow patches: Statistical properties, IMF dependence, and contribution to polar cap convection. *Journal of Geophysical Research: Space Physics*, *120*(5), 4064–4078. doi: 10.1002/2014JA020946